Effect of Iron Impurities on Magnetic Properties of Nanosized CeO$_2$ and Ce-Based Compounds

Yvonna Jiraskova [1],*, **Jiri Bursik** [1], **Pavel Janos** [2], **Jiri Lunacek** [3], **Artur Chrobak** [4] **and Ondrej Zivotsky** [3]

[1] CEITEC IPM, Institute of Physics of Materials, AS CR, Zizkova 22, 616 62 Brno, Czech Republic; bursik@ipm.cz

[2] Faculty of the Environment, University of Jan Evangelista Purkyne, Kralova Vysina 7, 400 96 Usti nad Labem, Czech Republic; pavel.janos@ujep.cz

[3] Department of Physics, VSB-Technical University of Ostrava, 17.listopadu 15, 708 33 Ostrava-Poruba, Czech Republic; jiri.lunacek@vsb.cz (J.L.); ondrej.zivotsky@vsb.cz (O.Z.)

[4] Institute of Physics, University of Silesia in Katowice, Pułku Piechoty 1A, 41-500 Chorzów, Poland; artur.chrob@gmail.com

* Correspondence: jirasko@ipm.cz; Tel.: +420-532290446

Abstract: CeO$_2$ samples prepared by three technological procedures from the same cerium source, namely cerium (III) nitrate hexahydrate, are studied from the viewpoint of structure, chemical and phase composition, and micro- and macro-magnetic properties. The scanning and transmission electron microscopies completed by energy-dispersive X-ray (EDX) analysis yield nano-structural natures and homogenous chemical compositions of the ceria samples, confirmed also by X-ray diffraction. The diamagnetic, paramagnetic, and ferromagnetic phases in all samples follow from an analysis of the room- and low-temperature measurements of hysteresis loops. Iron impurities in ppm amounts are clearly detected by ^{57}Fe Mössbauer spectrometry not only in the ceria samples but also in the selected input chemicals used for their preparation. This contributes to the explanation of the magnetic behaviour of nanosized ceria.

Keywords: CeO$_2$; microstructure; magnetic properties; Mössbauer spectrometry

1. Introduction

Cerium, the chemical element with atomic number 58, is a silver-white metal and the second element in the lanthanide series. It shows +3 and +4 oxidation states. The most widely used compound of cerium is cerium oxide CeO$_2$, known also as ceria. It crystallises in the fluorite crystal structure with space group Fm$\overline{3}$m (Figure 1) over the temperature range from room temperature to the melting point. The fluorite structure consists of a face-centred cubic (f.c.c.) unit cell of cations, with anions occupying the tetrahedral interstitial sites. This can also be seen as a superposition of a f.c.c. lattice of cations (Ce^{4+}) with lattice constant a and a simple cubic lattice of anions (O^{2-}) with lattice constant $a/2$. In this structure, each cerium cation is coordinated by eight nearest-neighbour oxygen anions, while each oxygen anion is coordinated by four nearest-neighbour cerium cations [1]. The colour of CeO$_2$ is pale yellow. The CeO$_2$ nanoparticles can be synthesised by solution-based methods including co-precipitation, micro-emulsion processes, sol-gel techniques, combustion reaction, etc.
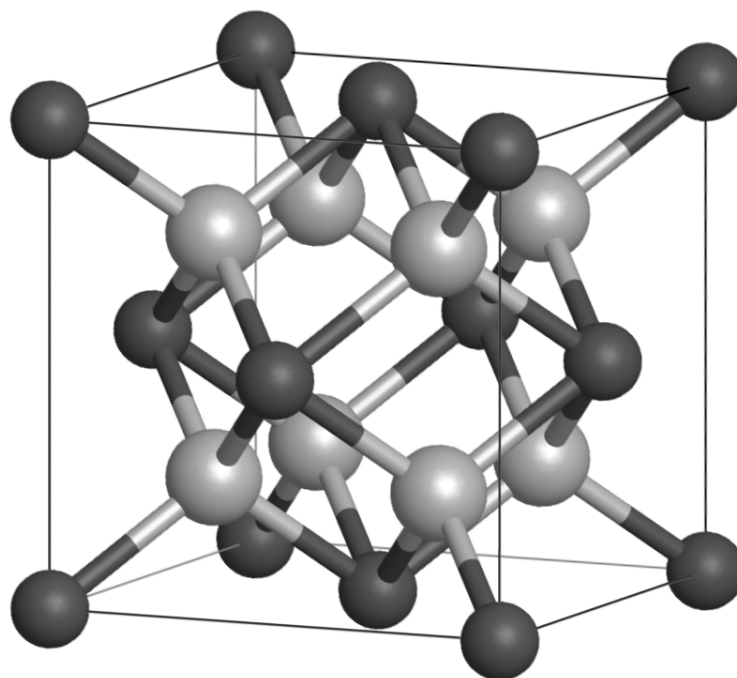
Figure 1. Fluorite-type crystal structure of CeO$_2$ (Ce atoms are in dark grey and O atoms are in light grey).

Ceria is presently a frequently studied compound because of its unique physical properties, which offer a number of various applications. It is extensively used as a catalyst in various chemical processes, e.g., for the elimination of toxic auto-exhaust gases [2,3], as a glass-polishing material [4], or in biotechnology, environmental chemistry, and medicine [5,6]. The mobility of oxygen vacancies and consequently the high ionic conductivity determines ceria as a promising electrolyte for solid oxide fuel cells [7] and other applications [8]. Just the oxygen vacancies and their effects on the magnetic properties of ceria and some other nonmagnetic oxides, such as Al$_2$O$_3$ or ZnO, call for deeper investigations. The main reason is the puzzling large difference in obtained magnetic moments presented by authors all over the world. The origin of magnetic moments in these oxides, predominantly in their nano-sized form, is ascribed to a formation of localised electron spin moments at the oxygen vacancies particularly present at nano-particle surfaces. In the case of CeO$_2$, another reason for its ferromagnetic behaviour has to be considered, namely the effects of Ce^{3+} ions on the nano-particle surfaces which, contrary to diamagnetic Ce^{4+} ions, carry their own magnetic moments. Recently, the magnetic behaviour of nanosized ceria has also been ascribed to a presence of a small amount of magnetic iron-based impurities. Their amount in units of ppm was detected by low-temperature magnetic measurements using a superconducting quantum interference device (SQUID) magnetometer and subsequently confirmed by ^{57}Fe Mössbauer spectrometry, which is highly sensitive to the presence of iron atoms in a compound [9]. Nevertheless, some Ce-based compounds yield a relatively high magnetic moment even if no iron is detected by Mössbauer spectrometry. Therefore, the present study is concentrated on ceria prepared by different technological procedures. It continues our previous investigations [9,10] in order to shed more light on the magnetic behaviours of ceria and Ce-compounds. The nano-sized CeO$_2$ powders were prepared from the same cerium (III) nitrate hexahydrate using three precipitation procedures with different chemicals. Their structural and physical analyses were completed by analysing selected chemicals used for CeO$_2$ production from the viewpoint of possible iron and/or other chemical element contaminations.

2. Materials and Methods

Three cerium oxide samples, denoted as S4, S5, and S6, were prepared from the same cerium source (cerium (III) nitrate hexahydrate, 99.0%, Sigma-Aldrich) using different precipitation procedures. The sample S4 was prepared by conventional direct precipitation of the cerous nitrate solution with the saturated solution of oxalic acid, whereas the sample S5 was prepared by homogeneous precipitation with dimethyl oxalate [11]. In both cases, the resulting cerous oxalates were dried and annealed at 500 °C for 2 h in air to convert them into cerium oxides. The sample S6 was prepared by a well-established precipitation/calcination synthetic route [12,13] using ammonium carbonate as a precipitant, with subsequent calcination at 500 °C. Oxalic acid, dimethyl oxalate, and ammonium bicarbonate were obtained from Sigma-Aldrich as reagent-grade chemicals with purity above 99%. All solutions were prepared in deionised water obtained from a Demi Ultra 20 system (Goro, Prague, Czech Republic), in which reverse osmosis and mixed-bed ion-exchange were used for water purification.

The selected chemicals were subjected to supplementary chemical and/or magnetic analysis. Cerous nitrate 5N–N (CeN) of purity 99.999% (Sigma-Aldrich) was analyzed using the Inductively Coupled Plasma Atomic Emission Spectroscopy (ICP-AES), and the content of iron was determined to be 3.61 ppm. This method was also used for cerous chloride 3N–C (denoted CeCl) of purity 99.9% (Sigma-Aldrich), which is similarly frequently used for CeO_2 production, and the content of Fe was 2.83 ppm. Both values are comparable with 1.78 ppm obtained for cerium (III) nitrate hexahydrate 99.0% used for the preparation of the S4, S5, and S6 samples.

The morphologies and microstructures of the samples were investigated using a TESCAN LYRA 3XMU FEG/SEM scanning electron microscope (SEM, Brno, Czech Republic) operated at an accelerating voltage of 20 kV. The microscope was also equipped with an XMax80 Oxford Instruments detector (UK) for energy-dispersive X-ray (EDX) analysis. The structure in the nano-size dimension was observed by a transmission electron microscope (TEM) Philips CM12 STEM (Amsterdam, The Netherlands) with a thermoemission electron source operating at 120 kV. The powder samples for SEM observation were prepared by spreading a small amount of powder onto a sticky conductive tape, and those for TEM were treated ultrasonically in an ethanol bath for 5 min and then placed on holey carbon copper grids.

X-ray diffraction (XRD) patterns were measured at room temperature (RT) using an X'PERT PRO diffractometer with Co Kα radiation ($\lambda = 0.17902$ nm) in the 2θ range from 20° to 135° in steps of 0.01° and time per step of 5 s. The evaluation of powder patterns was realised by the Rietveld structure refinement method [14] in semi-automatic mode, using the HighScore Plus program Version 4.8.0 (Malvern Panalytical, UK) and the ICSD database (FIZ Karlsruhe, Germany) of inorganic and related structures [15]. The pattern analysis yielded the phase composition, lattice parameters, and the mean crystallite size, representing a size of coherently diffracting domains.

Room- and low-temperature (RT, LT) hysteresis loops were measured using the Quantum Design XL-7 superconducting quantum interference device (SQUID) magnetometer (Quantum Design, CA, USA). Special care was devoted to the sample holder and to the sample handling procedures, to prevent any contamination of the holder as well as the samples. The saturation magnetisation was derived from the hysteresis loops at an accuracy of approximately ±1%.

The Mössbauer spectrometry was used to detect and/or exclude the contamination of the samples with iron impurities. The measurements were performed at RT in standard transmission geometry using ^{57}Co(Rh) source. Calibration of the velocity scale was performed with α-Fe at RT and the isomer shifts are given with respect to its Mössbauer spectrum. All spectra were evaluated using the transmission integral approach in the program CONFIT [16]. The experimental points were analysed by double- and single-line components yielding values of isomer shift (δ) and quadrupole splitting (Δ). The relative representation of these subcomponents is denoted by A.

3. Results and Discussion

3.1. Morphology, Phase, and Chemical Composition

The morphologies of samples obtained using SEM are shown in Figure 2 (left panel). The EDX chemical analysis has not detected any other elements besides Ce and oxygen (with a usual EDX inaccuracy in light element quantification). Both integral (area of approx. 1 mm^2) and point chemical analyses in all three samples were done from several places, and the mean values summarised in Table 1 do not yield any systematic difference. Similarly, there is no important difference in microstructure among the samples and, therefore, the TEM observation was done for the S6 sample only and the resulting fine nanostructure, including confirmation of CeO$_2$ f.c.c. crystal structure by the diffraction pattern, is seen in Figure 3. The TEM micrograph clearly shows that the particle size ranges between approximately 10 and 50 nm.
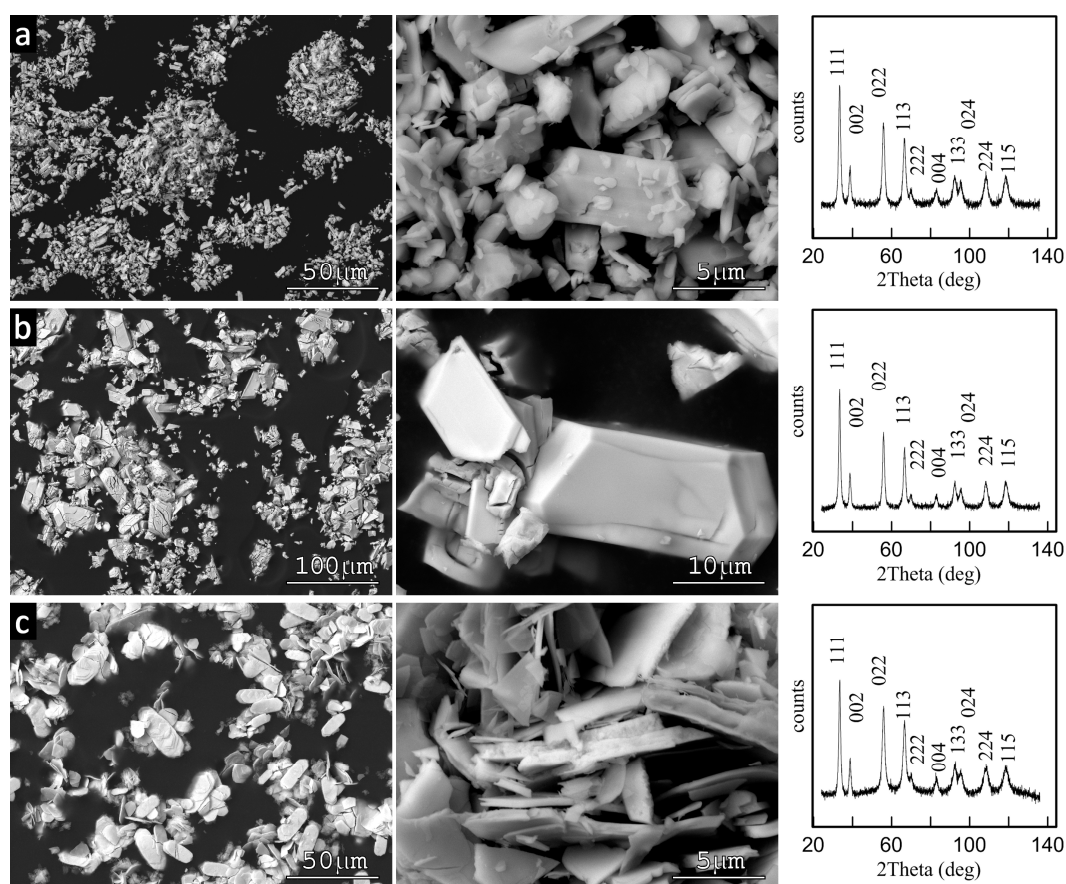

Figure 2. Left panel: SEM morphology of the cerium oxide samples S4 (**a**), S5 (**b**), and S6 (**c**). Right panel: X-ray diffraction patterns.

Table 1. Mean chemical composition (at. %) of the S4, S5, and S6 samples obtained by energy-dispersive X-ray (EDX) analysis.

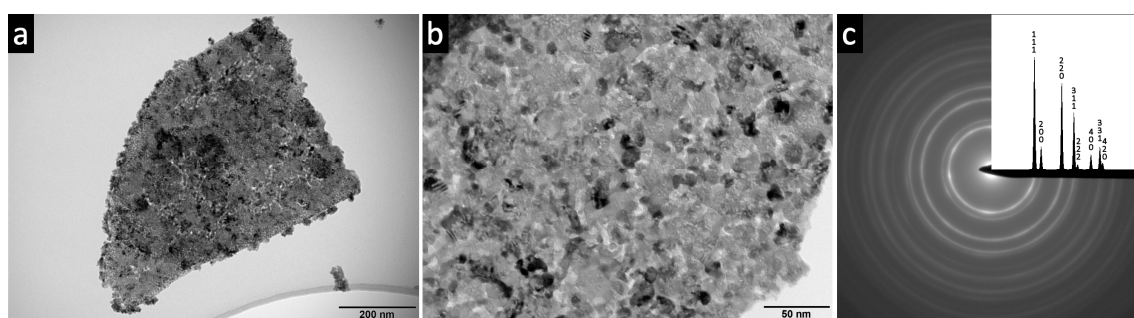| Sample/Element		Area		Point	
S4	Ce	28.4	±4.6	19.1	±4.1
	O	71.6		80.9	
S5	Ce	28.6	±0.2	24.8	±5.0
	O	71.4		75.2	
S6	Ce	27.9	±0.4	26.2	±2.7
	O	72.1		73.8	

Figure 3. TEM micrographs of the S6 sample nanostructure (**a**,**b**) and diffraction with analysed face-centred cubic (f.c.c.) CeO_2 phase (**c**).

The electron microscope observations are in good agreement with X-ray diffraction measurements. The patterns of all samples depicted in Figure 2 (right panel) were analysed by the same ICSD 28753 data sheet for the 225 (Fm$\bar{3}$m) space group, and the denoted (hkl) peaks are practically identical. They represent the CeO_2 phase. The lattice parameters for S4, S5, and S6 samples: 0.5414(1) nm, 0.5413(1) nm, and 0.5415(1) nm, respectively, are identical in the frame of accuracy of measurement. A slight difference is observed only in the crystallite (microdomain) size, *d*, calculated using the Scherrer formula employing parameters of (111) peak: *d* = 15.1 nm for S4, *d* = 21.8 nm for S5, and *d* = 19.01 nm for S6. These results point out the nanocrystalline nature of studied samples and confirm the representative TEM result in Figure 3, rather than quite large CeO_2 plates (seemingly single crystals) shown by SEM in Figure 2 (left panel).

3.2. Macroscopic Magnetic Properties

The hysteresis curves of the S4, S5, and S6 samples measured at RT are presented in Figure 4 (left panel) and those obtained at a low temperature of 2 K are summarised in the middle panel. They consist of diamagnetic, paramagnetic, and ferromagnetic contributions. The diamagnetic contribution is reflected at all hysteresis loops by a decrease of magnetisation at higher magnetic fields. It is described by a negative magnetic susceptibility, χ_D, practically independent on the applied temperature. Estimated values of χ_D of the studied samples are summarised in Table 2. A sharp magnetisation reversal at lower magnetic fields seen at the RT hysteresis loops in Figure 4 (left panel) is indicative of the ferromagnetic contribution. This can originate in a large number of structural defects, particularly surface oxygen vacancies mentioned by some authors [17–21], and/or magnetic impurities, namely iron [9,10] contributing to small values of RT ferromagnetic saturation magnetisation of an order of 10^{-3} Am^2/kg, detected also in other usually nonmagnetic compounds [22]. The analysis of the present magnetic measurements of the S4, S5, and S6 samples has resulted in the detection of a small amount of iron impurities, in units of ppm as seen in Table 2.

The paramagnetic contribution is practically hidden in the RT measurements, but it can be well determined from the LT curves. Contrary to the diamagnetic contribution, the paramagnetic contribution following the Curie–Weiss law is strongly dependent on temperature. It could be determined from the LT hysteresis loops in Figure 4 (middle panel) after a subtraction of the diamagnetic and ferromagnetic contributions. This has resulted in magnetisation curves in Figure 4 (right panel) that are compared with the Brillouin function (dash-dotted line) calculated using a total electronic angular momentum *J* = 5/2 and the Lande's *g*-factor *g* = 6/7. The estimated saturation paramagnetic moment M_{spm} (Table 2) can be converted to the Bohr magneton per formula unit ($M_{spm}/12$), and then compared with the theoretical saturation moment of Ce^{3+} ions equal to 2.54 μ_B. This resulted in a low concentration of the Ce^{3+} ions in all samples, reaching about 10^{-3}, which is substantially less compared to the diamagnetic Ce^{4+} ions.
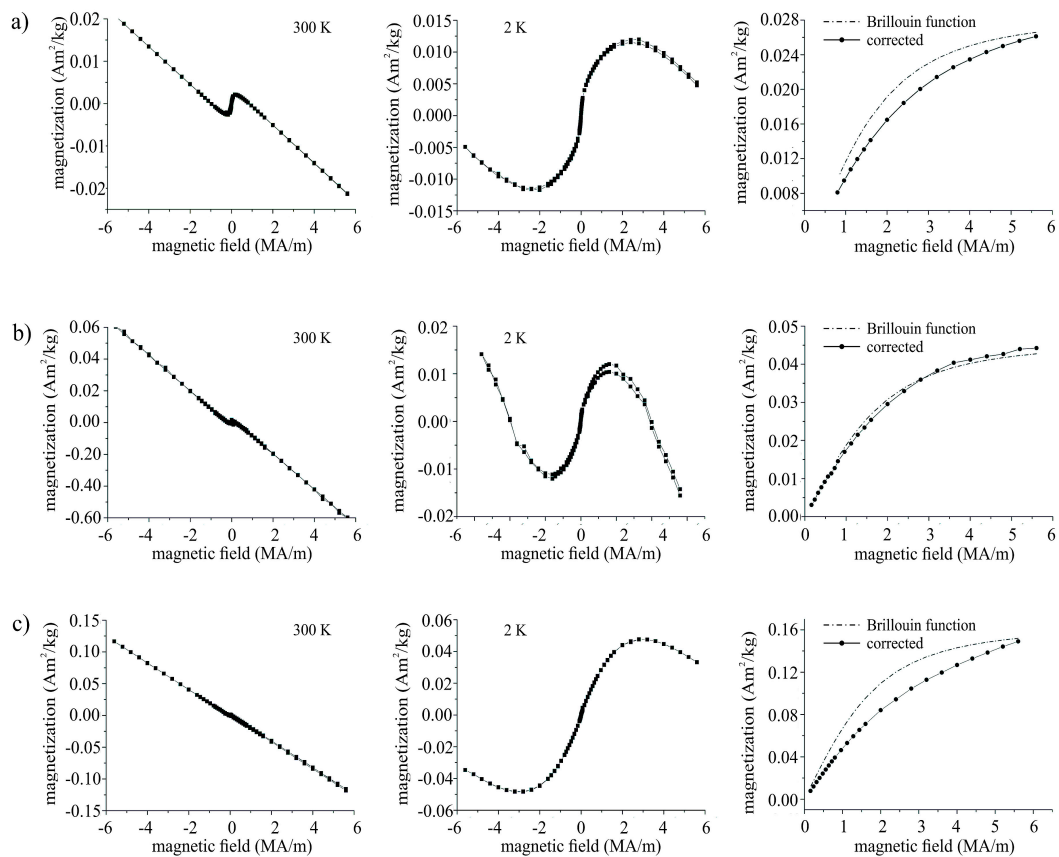
Figure 4. Measured hysteresis loops at 300 K (left panel) and 2 K (middle panel) of the S4 (**a**), S5 (**b**), and S6 (**c**) samples. Paramagnetic contribution is obtained after diamagnetic and ferromagnetic correction and compared to the Brillouin function (right panel).

Table 2. Parameters determined from the magnetic measurements and from the Brillouin function: χ_D—diamagnetic susceptibility established from 300 K and 2 K hysteresis loops; M_{sfm} 300 K—saturation magnetisation of ferromagnetic contribution at 300 K; M_{spm} 2 K—saturation magnetisation of paramagnetic contribution at 2 K.

Sample	χ_D (m^3/kg)	M_{sfm} **300 K** (Am^2/kg)	**Fe Content (ppm)**	M_{spm} **2 K** (Am^2/kg)	Ce^{3+} **Concentration (-)**
S4	$-4.5 \cdot 10^{-9}$	0.0020	9	0.028	0.0009
S5	$-1.1 \cdot 10^{-8}$	0.0008	3	0.045	0.0015
S6	$-2.1 \cdot 10^{-8}$	0.0014	6	0.160	0.0052

As it was mentioned above, the selected chemicals, namely those at which the iron impurities were evidenced by ICP-AES analysis, were studied by magnetic techniques as well. The small amounts of iron impurities (2.83 ppm in CeN and 3.61 ppm in CeCl) have caused a weak magnetisation reversal at the room temperature and at the low applied fields. This was similar to ferromagnetic contributions detected in the CeO_2 samples. Moreover, the RT hysteresis loops (not presented here) exhibited paramagnetic responses with mass magnetisation of about 0.3–0.5 Am^2/kg at magnetic fields of 5.6 MA/m (7 T), and mass susceptibilities of 5×10^{-8} m^3/kg for CeN and of 6×10^{-8} m^3/kg for CeCl. The much stronger paramagnetic moment of about 15–20 Am^2/kg was obtained from the hysteresis loops measured at the low temperature of 2 K. Based on the certificates mentioning cerium occurring in combination with other lanthanide impurity elements, the strong paramagnetic moment was successfully analyzed by the Brillouin function of neodymium ($J = 4$, $g = 0.603$) and/or praseodymium ($J = 4.5$, $g = 0.732$) overlapping the magnetically poor response of cerium.

3.3. Mössbauer Spectrometry

The Mössbauer spectrometry was used to verify a presence of iron in the samples and selected chemicals frequently used in the production of cerium oxide. The measured and analysed Mössbauer spectra in Figure 5a clearly prove a presence of iron in all three samples. The lower effect of measurements of coarser powders of the chemicals (Figure 5b) has evoked extended times of data reading. Nevertheless, the spectra confirm a presence of iron in the chemicals as well. A slightly better effect, observed at CeN, corresponds to the higher Fe content followed from the ICP-AES. The spectra of the samples were evaluated using one double-line component with hyperfine parameters (isomer shift, δ, and quadrupole slitting, Δ) not too different in the frame of experimental errors: S4: δ = 0.229(10) mm/s, Δ = 0.316(15) mm/s; S5: δ = 0.251(19) mm/s, Δ = 0.303(34) mm/s; and S6: δ = 0.232(12) mm/s, Δ = 0.333(18) mm/s. The spectra of chemicals were analysed using the singlet of δ = 0.218(68) mm/s for CeCl and δ = 0.374(31) mm/s for CeC, and a doublet for CeN of δ = 0.397(43) mm/s and Δ = 0.118(106) mm/s. Though the measurements are limited by the sensitivity of the Mössbauer effect, they support the magnetic results and confirm well the chemical analysis yielding small amounts of iron (see Section 2). They are not substantially different from the previous findings presented in Refs. [9,10].

It is also evident that the preparation of the "iron-free" cerium oxide would require more sophisticated synthetic routes and/or a utilisation of the iron-free starting materials. Although some of the used procedures are recommended for the separation of rare earths from common metals (precipitation of oxalates) [23], they are obviously unable to remove the residual amounts of iron from cerium at the ppm level completely.
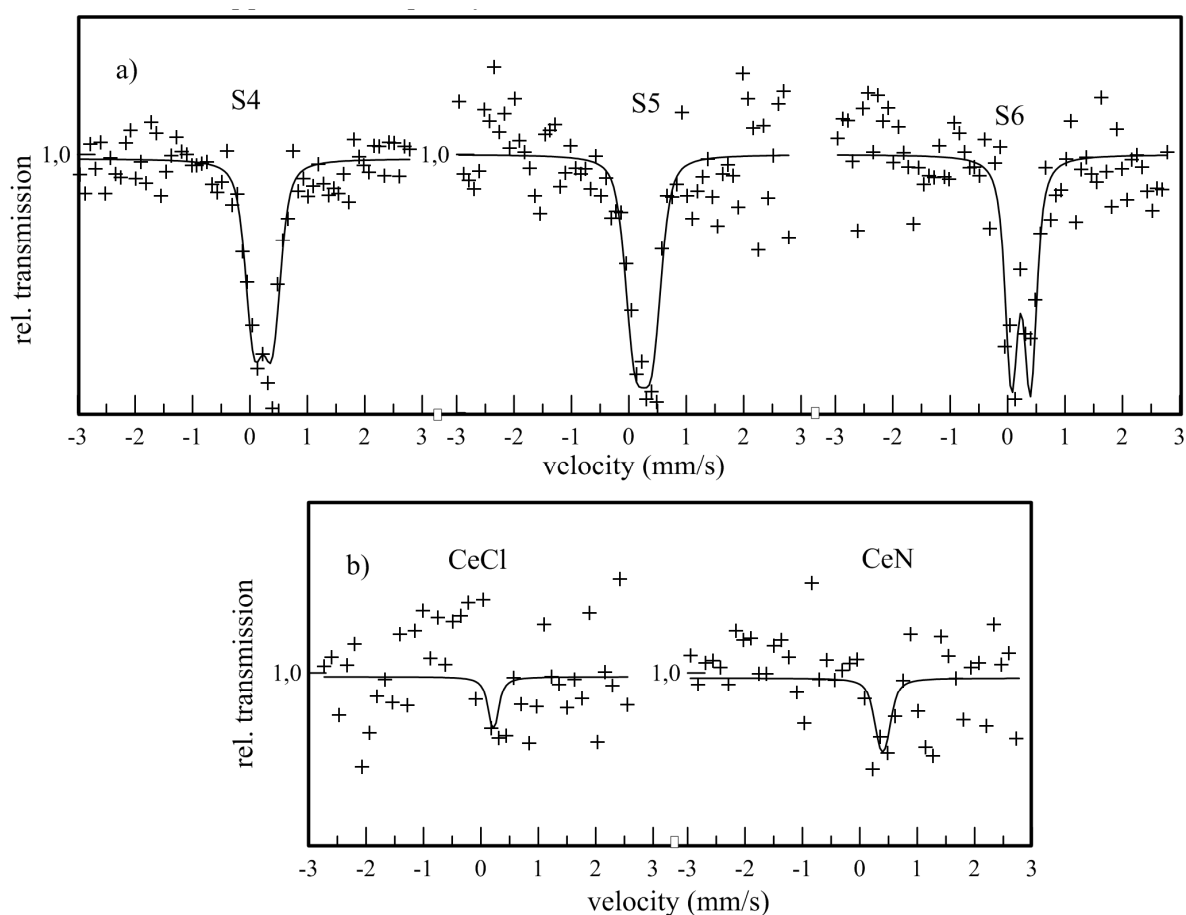

Figure 5. Room temperature Mössbauer spectra (**a**) of the S4, S5, and S6 samples prepared from different chemicals and (**b**) of selected chemicals, cerous chloride (CeCl) and cerous nitrate (CeN).

4. Conclusions

The study is devoted to a clarification of the magnetic behaviour of ceria in its nano- up to micro-sized forms. The room- and low-temperature magnetic measurements of the samples prepared from the cerium (III) nitrate hexahydrate source and using three different precipitation reactions clearly prove the presence of the diamagnetic, paramagnetic, and ferromagnetic phases. While the effect of Ce^{3+} ions as carriers of their own magnetic moments can be excluded due to their insignificant concentration compared to diamagnetic Ce^{4+} ions in ceria, the iron impurities detected by chemical analysis, reflected in hysteresis loops, and confirmed by Mössbauer spectrometry play a significant role despite their small amount. Their well-established presence in ceria excludes the effect of oxygen vacancies as a unique source of ceria magnetism.

As follows from the present ICP-AES analyses and from certificates provided by the supplier, the raw materials (Ce sources) for the ceria preparation contained trace amounts of iron, typically at the level of several ppm, that was also confirmed by other experimental methods used here. Similarly, the precipitating agents were also not completely iron-free. For example, the content of iron in oxalic acid and ammonium carbonate ranges between 2 and 5 ppm according to specifications, and a similar value may be expected also in dimethyl oxalate. This raises a question of whether it is in general possible to produce ceria free of iron, in spite of the synthetic routes (especially those utilising oxalic acid and dimethyl oxalate) which are declared as highly selective separation methods for the rare earths purification. The effect of neodymium and/or praseodymium, detected in the chemicals, on the magnetic behaviour of ceria also remains unclear.

Author Contributions: Sample preparation, P.J.; electron microscope observations. J.B.; SQUID magnetic measurements, A.C.; room-temperature magnetic measurements, O.Z.; magnetic curve analysis, O.Z. and J.L.; XRD and Mössbauer measurements, Y.J.; manuscript preparation, Y.J.; manuscript editing, J.B., O.Z., and J.L.

Conflicts of Interest: The authors declare no conflict of interest.

References

1. Schwarz, K. Materials design of solid electrolytes. *Proc. Natl. Acad. Sci. USA* **2006**, *103*, 3497. [CrossRef] [PubMed]
2. Alikin, E.A.; Vedyagin, A.A. High Temperature Interaction of Rhodium with Oxygen Storage Component in Three-Way Catalysts. *Top. Catal.* **2016**, *59*, 1033–1038. [CrossRef]
3. Trovarelli, A. Catalytic properties of ceria and CeO_2-containing materials. *Catal. Rev.* **1996**, *38*, 439–520. [CrossRef]
4. Armini, S.; De Messenmaeker, J.; Whelan, C.M.; Moinpour, M.; Maex, K. Composite polymer core-ceria shell abrasive particles during oxide CMP: A defectivity study. *J. Electrochem. Soc.* **2008**, *155*, H653–H660. [CrossRef]
5. Tarnuzzer, R.W.; Colon, J.; Patil, S.; Seal, S. Vacancy engineered ceria nanostructures for protection from radiation-induced cellular damage. *Nano Lett.* **2005**, *5*, 2573–2577. [CrossRef] [PubMed]
6. Asati, A.; Santra, S.; Kaittanis, C.; Nath, S.; Perez, J.M. Oxidase-Like Activity of Polymer-Coated Cerium Oxide Nanoparticles. *Angew. Chem.* **2009**, *48*, 2308–2312. [CrossRef] [PubMed]
7. Park, S.D.; Vohs, J.M.; Gorte, R.J. Direct oxidation of hydrocarbons in a solid-oxide fuel cell. *Nature* **2000**, *404*, 265–267. [CrossRef] [PubMed]
8. Younis, A.; Chu, D.; Li, S. Cerium Oxide Nanostructures and their Applications. In *Functionalized Nanomaterials*; Farrukh, M.A., Ed.; IntechOpen: Rijeka, Croatia, 2016; pp. 53–68. [CrossRef]
9. Lunacek, J.; Zivotsky, O.; Janos, P.; Dosek, M.; Chrobak, A.; Marysko, M.; Jiraskova, Y. Structure and magnetic properties of synthesized fine cerium dioxide nanoparticles. *J. Alloys Comp.* **2018**, *753*, 167–175. [CrossRef]
10. Jiraskova, Y.; Bursik, J.; Zivotsky, O.; Lunacek, J.; Janos, P. Magnetic and Mossbauer Study of Cerium-Based Reactive Sorbent. *Acta Phys. Pol. A* **2017**, *131*, 1096–1098. [CrossRef]

11. Salutsky, M.L.; Kirby, H.W. Precipitation of actinium oxalate from homogeneous solution. *Anal. Chem.* **1956**, *28*, 1780–1782. [CrossRef]

12. Janos, P.; Kuran, P.; Kormunda, M.; Stengl, V.; Grygar, T.M.; Dosek, M.; Stastny, M.; Ederer, J.; Pilarova, V.; Vrtoch, L. Cerium dioxide as a new reactive sorbent for fast degradation of parathion methyl and some other organophosphates. *J. Rare Earths* **2014**, *32*, 360–370. [CrossRef]

13. Janos, P.; Henych, J.; Pelant, O.; Pilarova, V.; Vrtoch, L.; Kormunda, M.; Mazanec, K.; Stengl, V. Cerium oxide for the destruction of chemical warfare agents: A comparison of synthetic routes. *J. Hazard. Mater.* **2016**, *304*, 259–268. [CrossRef] [PubMed]

14. Young, R.A. (Ed.) *The Rietveld Method*; International Union of Crystallography, Oxford University Press Inc.: New York, NY, USA, 1993.

15. *ICSD Database*, Version 1.9.4; NIST/FIZ; FIZ Karlsruhe: Karlsruhe, Germany, 2014; Volume 1.

16. Zak, T.; Jiraskova, Y. CONFIT: Mossbauer spectra fitting program. *Surf. Interface Anal.* **2006**, *38*, 710–714. [CrossRef]

17. Il'ves, V.G.; Sokovnin, S.Y. Production and studies of properties of nanopowders on the basis of CeO_2. *Nanotechnol. Rus.* **2012**, *7*, 213–226. [CrossRef]

18. Ge, M.Y.; Wang, H.; Liu, E.Z.; Liu, J.F.; Jiang, J.Z.; Li, Y.K.; Xu, Z.A.; Li, H.Y. On the origin of ferromagnetism in CeO(2) nanocubes. *Appl. Phys. Lett.* **2008**, *93*, 062505. [CrossRef]

19. Chen, S.Y.; Lu, Y.H.; Huang, T.W.; Yan, D.C.; Dong, C.L. Oxygen Vacancy Dependent Magnetism of CeO_2 Nanoparticles Prepared by Thermal Decomposition Method. *J. Phys. Chem. C* **2010**, *114*, 19576–19581. [CrossRef]

20. Sundaresan, A.; Bhargavi, R.; Rangarajan, N.; Siddesh, U.; Rao, C.N.R. Ferromagnetism as a universal feature of nanoparticles of the otherwise nonmagnetic oxides. *Phys. Rev. B* **2006**, *74*, 161306. [CrossRef]

21. Sundaresan, A.; Rao, C.N.R. Ferromagnetism as a universal feature of inorganic nanoparticles. *Nano Today* **2009**, *4*, 96–106. [CrossRef]

22. Esquinazi, P.; Setzer, A.; Höhne, R.; Semmelhack, C.; Kopelevich, Y.; Spemann, D.; Butz, T.; Kohlstrunk, B.; Losche, M. Ferromagnetism in oriented graphite samples. *Phys. Rev. B* **2002**, *66*, 024429. [CrossRef]

23. Abreu, R.D.; Morais, C.A. Purification of rare earth elements from monazite sulphuric acid leach liquor and the production of high-purity ceric oxide. *Miner. Eng.* **2010**, *23*, 536–540. [CrossRef]